

A second visit to Eps Ind Ab with JWST: new photometry confirms ammonia and suggests thick clouds in the exoplanet atmosphere of the closest super-Jupiter.

ELISABETH C. MATTHEWS ¹, JAMES MANG ^{2,*}, AARYNN L. CARTER ³, MATHLIDE MÂLIN ³,
CAROLINE V. MORLEY ², BHAVESH RAJPOOT ^{1,4}, LEINDERT A. BOOGAARD ⁵, JENNIFER A. BURT ⁶,
IAN J. M. CROSSFIELD ⁷, FABO FENG ⁸, ANNE-MARIE LAGRANGE ⁹, AND MARK W PHILLIPS ¹⁰

¹Max Planck Institute for Astronomy, Königstuhl 17, D-69117 Heidelberg, Germany

²Department of Astronomy, University of Texas at Austin, 2515 Speedway, Austin, TX 78712, USA

³Space Telescope Science Institute, 3700 San Martin Drive, Baltimore, MD 21218, USA

⁴Department of Physics and Astronomy, Heidelberg University, Im Neuenheimer Feld 226, D-69120 Heidelberg, Germany

⁵Leiden Observatory, Leiden University, PO Box 9513, NL-2300 RA Leiden, The Netherlands

⁶Jet Propulsion Laboratory, California Institute of Technology, 4800 Oak Grove Drive, Pasadena, CA 91109, USA

⁷Department of Physics and Astronomy, University of Kansas, Lawrence, KS, USA

⁸Shanghai Jiao Tong University, Shengrong Road 520, Shanghai, 201210, People's Republic Of China

⁹LESIA, Observatoire de Paris, Université PSL, CNRS, 5 Place Jules Janssen, 92190 Meudon, France

¹⁰Institute for Astronomy, University of Edinburgh, Royal Observatory, Blackford Hill, Edinburgh EH9 3HJ, UK

(Accepted March 8, 2026)

ABSTRACT

With JWST, we are directly imaging cold ($\sim 200\text{--}300\text{K}$), solar-age giant exoplanets for the first time. At these temperatures many molecular features appear and water-ice clouds may condense and affect the emission spectrum; early photometric measurements of cold giant planets are already showing some tension with the predictions of cloud-free, solar-metallicity atmosphere models. Here we present new JWST/MIRI coronagraphic observations of the cold giant exoplanet Eps Ind Ab at $11.3\mu\text{m}$. Together with archival data, we use these new observations to study the atmosphere of this cold exoplanet, and we also re-fit its orbit, finding an updated mass of $7.6 \pm 0.7 M_{\text{Jup}}$ and an eccentricity of $0.24^{+0.11}_{-0.08}$. The planet is significantly brighter (by 0.88 ± 0.08 mag) at $11.3\mu\text{m}$ than at $10.6\mu\text{m}$, indicating the presence of ammonia. However, this ammonia feature is shallower than expected. This could indicate a low-metallicity or nitrogen-depleted atmosphere, but our preferred explanation is the presence of thick water-ice clouds that suppress the ammonia feature and the near-IR emission of Eps Ind Ab. Photometry of the small but growing sample of cold, giant exoplanets demonstrates that they are consistently fainter than expected between 3 to $5\mu\text{m}$, consistent with the water-ice cloud hypothesis. $10.6\mu\text{m}$ and $11.3\mu\text{m}$ photometry of this cold exoplanet sample would be valuable to determine whether the suppressed ammonia feature is universal, and to frame a new open question about the underlying physical cause.

Keywords: Extrasolar gaseous giant planets (2172) — Exoplanet atmospheres (487) — Exoplanet atmospheric composition (2021) — Y-type brown dwarfs (1827) — Coronagraphic imaging (2369)

1. INTRODUCTION

Through high-contrast imaging of nearby stars, it is possible to study the atmospheric abundances of their long-period exoplanets with photometric and spectro-

scopic campaigns. The James Webb Space Telescope (JWST), with its suite of coronagraphic instruments (J. J. Green et al. 2005; J. E. Krist et al. 2009; M. D. Perrin et al. 2018; D. Rouan et al. 2000; A. Boccaletti et al. 2022), provides a number of advantages in this regard. JWST allows for exquisite photometric precision, and it provides access to the mid-infrared – including the $10\text{--}11\mu\text{m}$ region where ammonia has significant opacity. Further, JWST uniquely opens the possibility to image

Corresponding author: Elisabeth C. Matthews
Email: matthews@mpia.de

* NSF Graduate Research Fellow.

cold exoplanets (<500 K), which are not currently accessible with ground-based imaging (e.g. B. P. Bowler 2016). To date, three of these cold exoplanets around main-sequence stars have been imaged with JWST: Eps Ind Ab (E. C. Matthews et al. 2024), 14 Her c (D. C. Bardalez Gagliuffi et al. 2025), and the candidate planet TWA 7b (A. M. Lagrange et al. 2025; K. A. Crotts et al. 2025). A few free-floating brown dwarfs (e.g. M. C.ushing et al. 2011; K. L. Luhman 2014) have also been imaged in this temperature regime.

At these cold temperatures, strong ammonia features are expected, as has already been observed spectroscopically in cold brown dwarfs with Spitzer and JWST (e.g. T. L. Roellig et al. 2004; G. Suárez & S. Metchev 2022; S. A. Beiler et al. 2024). Considering exoplanet imaging, the JWST/MIRI coronagraphs are designed such that the narrowband F1065C and F1140C filters (wavelengths $10.6\mu\text{m}$ and $11.3\mu\text{m}$) sit inside and outside the prominent $10\text{--}11\mu\text{m}$ ammonia absorption feature, respectively. Photometry in both filters is thus sufficient to confirm the presence of ammonia in a cold exoplanet, and measure its abundance. This has been demonstrated on-sky in observations of GJ 504 b (M. Mâlin et al. 2025), which revealed the planet to have $F1065\text{C}\text{--}F1140\text{C} = 0.45 \pm 0.14$ mag. M. Mâlin et al. (2025) used these infrared measurements and archival data to confirm the first confident ($> 5\sigma$) detection of ammonia in an exoplanet. The ammonia feature is deeper in the mid-IR than the near-IR, and therefore appears already at warmer temperatures (see e.g. G. Suárez & S. Metchev 2022), but attempts have also been made to detect ammonia with near-IR observations (N. Whiteford et al. 2023; L. Welbanks et al. 2024).

The focus of the current work is Eps Ind Ab, a ~ 275 K planet first imaged by E. C. Matthews et al. (2024). That work presented exoplanet photometry at $10.6\mu\text{m}$ and $15.5\mu\text{m}$ (from JWST), as well as a low-significance photometric detection in a broadband $10.5\text{--}12.5\mu\text{m}$ VISIR/NEAR filter. Curiously, the exoplanet was not detected in archival VLT/NaCo observations (M. Janson et al. 2009; G. Viswanath et al. 2021), and this faint near-IR ($3\text{--}5\mu\text{m}$) flux is in tension with the predictions of most atmosphere models (M. W. Phillips et al. 2020; M. S. Marley et al. 2021). Sonora ElfOwl models (S. Mukherjee et al. 2024) with high metallicity and high C/O were found to be consistent with all in-hand photometry and upper limits of E. C. Matthews et al. (2024), but this composition would be somewhat surprising for a planet as massive as Eps Ind Ab since it requires a significant heavy-element content in the disk and efficient accretion of those heavy elements onto the planet. Planet formation studies predict C/O ratios

$\lesssim 1.5\times$ solar and metallicities within a few times solar for giant planets (e.g. K. I. Öberg et al. 2011; P. Mollière et al. 2022; A. B. T. Penzlin et al. 2024) and previous works have also found that more massive planets have metallicities closer to those of their host stars (e.g. D. P. Thorngren et al. 2016).

In this paper, we present a new epoch of JWST/MIRI coronagraphic observations of Eps Ind A. These were collected ~ 2 years after the first JWST observations, and in a new photometric filter (F1140C). We describe the new observations and data reduction in Sections 2 and 3. Combining the new and archival photometry, we see clear evidence for ammonia in the Eps Ind Ab atmosphere (Section 4). The ammonia feature is smaller than expected based on cloud-free, solar-metallicity models, and that the cold brown dwarf WISE 0855 has a similarly small ammonia feature: possibly indicating a universal trend in how ammonia features appear in the coldest substellar atmospheres and posing an open question as to the underlying physics causing this shallow ammonia feature; we explore several hypotheses in Section 4. We also demonstrate that the companion shows common proper motion with the host star (Section 5), as already suggested in E. C. Matthews et al. (2024), and re-fit the orbit of Eps Ind Ab (Section 6). Finally, in Section 7 we provide some discussion and concluding thoughts.

2. OBSERVATIONS

We observed Eps Ind A with the JWST/MIRI coronagraphic imager (A. Boccaletti et al. 2015, 2022) on 2025-05-10 (Program GO #5037, PI Matthews), using the F1140C filter and the four-quadrant phase-mask coronagraph (4QPM; D. Rouan et al. 2000). We collected observations of (a) the science target, (b) a PSF reference target so as to subtract the stellar PSF from observations with reference differential imaging (RDI; B. A. Smith & R. J. Terile 1984), using the 5-point small grid dither technique (R. Soummer et al. 2013; C.-P. Lajoie et al. 2016), and (c) two background fields so as to subtract the “glow stick” stray-light feature (A. Boccaletti et al. 2022) that appears in MIRI coronagraphic images. Observations of the two background field locations were designed to match the integration times of the science and PSF reference observations, and the fields are close to the science and PSF target respectively. Our chosen PSF target was DI Tuc (HD211055): this target was also used as a PSF reference star for the Eps Ind A observations collected in E. C. Matthews et al. (2024) and was demonstrated to be a suitable PSF reference target in that work. Full details of the observation sequence are provided in Table 1, and all JWST observations of

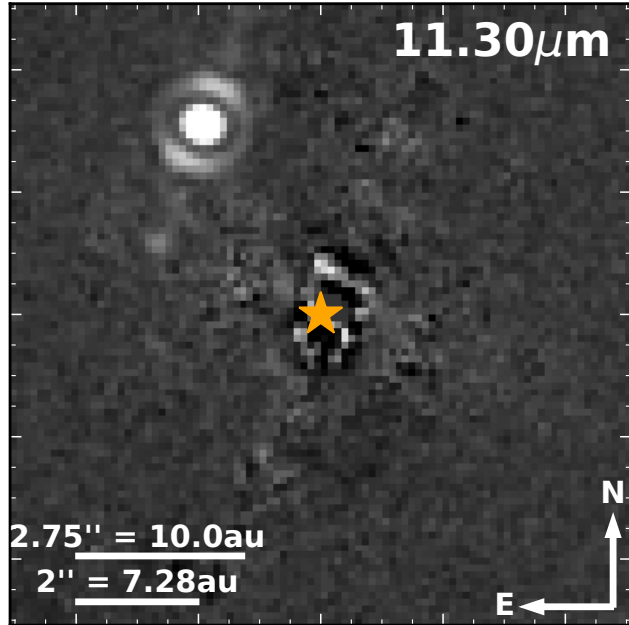


Figure 1. Coronagraphic images of Eps Ind A, collected with the F1140C filter of JWST/MIRI. The planet is detected as a bright point source in upper left of this image.

Eps Ind Ab used in this paper can be found in MAST at <https://doi.org/10.17909/zep8-1p53>.

3. DATA REDUCTION

To create science-ready images, we processed the data with `spaceKLIP`¹¹ (J. Kammerer et al. 2022; A. L. Carter et al. 2023), using largely the same method as in E. C. Matthews et al. (2024) which in turn follows A. L. Carter et al. (2023). We briefly summarize the key steps here. We started our reductions from the `*uncal.fits` files (rather than the processed `*cal.fits` files), since previous works have shown that adjusting pipeline parameters in the `jwst` pipeline (H. Bushouse et al. 2023) steps that produce `*cal.fits` files can improve the final data reduction (A. L. Carter et al. 2023). In the `*uncal.fits` files, raw telemetry data has been converted into fits header keywords but no other processing has been performed.

We ran `step1` of the pipeline using an increased jump rejection threshold of 8 so as to avoid flagging too many pixels as bad. For `step2` we used standard pipeline settings. We then cleaned badpixels from our images, using several techniques sequentially to remove them: we used the data quality flags, spatially and temporally searched for outliers, and sigma clipped the data,

as well as manually flagging and removing badpixels that were not detected by the pipeline. We also subtracted the background, following the custom approach described in N. Godoy et al. (2024), and masked some bright pixels in the core of the stellar PSF. Finally, we padded the frames and replaced NaN values within the images. Plate scale, orientation angle, and distortion were not derived independently, and we instead used the calibrations provided as default by the `jwst` pipeline (H. Bushouse et al. 2023) and the corresponding values in the FITS headers (PIXAR_A2, ROLL_REF, V3IYANG).

To remove the stellar PSF, we used the `pyKLIP` package (J. J. Wang et al. 2015) as implemented within `spaceKLIP`. This package uses `KLIP` (R. Soummer et al. 2012), a principal component analysis based method which builds a stellar PSF model empirically from several reference images, that can then be subtracted from science observations of interest. Our observing sequence included reference star images but not rotated images of the same target, so we carried out an RDI-only reduction, making use of all five dithered observations of the reference star. We explored various combinations of annuli, subsections and number of modes to remove starlight; in Figure 1 we show an image of the target using a single annulus and subsection, and with 50 Karhunen–Loève modes removed.

3.1. Photometry of Eps Ind Ab

For a companion as bright as Eps Ind Ab, photon noise is not the limiting uncertainty in measuring the companion photometry. Instead, systematics and calibration terms are important in driving the photometric uncertainty – and these can be difficult to determine, especially for coronagraphic observations (see e.g. A. Boccaletti et al. 2023; M. Málin et al. 2024). We therefore take care to derive photometry that is simultaneously (1) accurate and (2) has realistic uncertainties. We follow the approach of A. Boccaletti et al. (2023): we use several different methods to extract the photometry, and analyze the spread of results. Our adopted flux is the mean and standard deviation of the value measured with each method. This provides robust values and uncertainties, and additionally provides an independent verification of the host star magnitudes derived in the JWST filters in E. C. Matthews et al. (2024, see their Methods section) since only some methods take the host star photometry into account. We note however that some potential sources of systematics (e.g. on the stellar magnitude) would bias all measurements with a certain method equally, that is, they impact the measured apparent magnitude but not the measured color.

¹¹ <https://spaceklip.readthedocs.io/en/latest/>, commit a72c167

Table 1. JWST/MIRI observations of Eps Ind A taken for JWST program GO #5037.

| Target | Filter | Readout | Groups/Int | Ints/Exp | Dithers | Total Time [s] |
|--------------|--------|---------|------------|----------|---------|----------------|
| background_1 | F1140C | FASTR1 | 697 | 25 | 2 | 8364.3 |
| eps Ind A | F1140C | FASTR1 | 697 | 25 | 1 | 4182.2 |
| DI Tuc | F1140C | FASTR1 | 378 | 24 | 5 | 10899.4 |
| background_2 | F1140C | FASTR1 | 378 | 24 | 2 | 4359.8 |

NOTE—background_1 and background_2 are located close to eps Ind A and DI Tuc respectively, and were selected to be free of sources in the WISE catalog. All observations were carried out sequentially between 2025-05-09 to 2025-05-10.

For our final color determination, we therefore use the mean and standard deviation of the color measured with each method (rather than calculating the color from the adopted apparent magnitudes). For this work, we use three methods to measure magnitudes and colors: (1) `spaceKLIP` companion injection; (2) a simulation based on `STPSF`¹² (a tool that produces custom PSF models for JWST for a specified input spectrum and telescope set-up, M. D. Perrin et al. 2014), but implemented outside of `spaceKLIP` and run on a data reduction performed entirely independently of `spaceKLIP`, following M. Malin et al. (2024); (3) a method based on a contrast measured relative to the stellar flux and using target acquisition observations, as described in A. Boccaletti et al. (2023). We also update the photometry at F1065C and F1550C originally derived in E. C. Matthews et al. (2024), following the same methods, that is, combining the `spaceKLIP` photometry (as measured in E. C. Matthews et al. 2024) with newly derived values using the two additional methods so that the uncertainties are more conservative.

We provide the final photometric measurements and uncertainties for all filters in Table 2, where we additionally provide photometric measurements derived using each of the individual methods above. The adopted colors of the companion are F1065C-F1140C = 0.88 ± 0.08 mag and F1065C-F1550C = 1.92 ± 0.08 mag.

4. DETECTION OF AMMONIA

The F1065C-F1140C color of Eps Ind Ab is 0.88 ± 0.08 mag, i.e., the planet has an 11σ difference in apparent magnitude between $10.6\mu\text{m}$ and $11.3\mu\text{m}$. This significant planet brightness difference between observations in two neighboring filters is strong evidence for the presence of an ammonia absorption feature. Figure 2 shows the filter profiles for the three MIRI coronagraphic filters in which Eps Ind Ab has been observed, alongside the opacity as a function of wavelength of ammonia (from P. A. Coles et al. 2019). Ammonia ab-

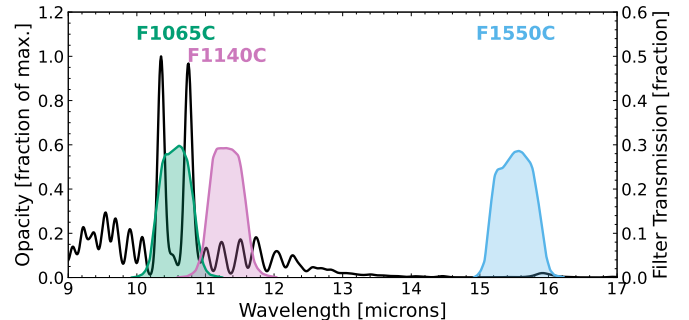


Figure 2. Opacity of ammonia as a function of wavelength (left axis), plotted against the transmission of the MIRI coronagraphic filters (right axis). The deep, double-peaked 10-11 μm ammonia absorption feature falls primarily in the F1065C filter, and the F1065C-F1140C color is a proxy for the depth of the feature.

sorbs strongly within the F1065C filter, but only weakly within the F1140C filter; consequently, a planet with a deep ammonia feature would show a significant difference in apparent magnitude between these two wavelengths.

To contextualize the measured photometry of Eps Ind Ab, we plot its position on color-magnitude diagrams (CMDs) in Figure 3, alongside the positions of a “default” atmosphere model from the Sonora Flame Skimmer model set (Mang et al. in prep.) with solar metallicity and carbon-to-oxygen ratio (C/O). Sonora Flame Skimmer is the next set of clear atmospheric and evolutionary models that extends the Sonora Bobcat (M. S. Marley et al. 2021) and Sonora Elf Owl (S. Mukherjee et al. 2024; N. F. Wogan et al. 2025) models to colder temperatures, a wider range of metallicities, and lower surface gravities. The Sonora Flame Skimmer grid spans $T_{\text{eff}} = 50\text{-}2400$ K, $\log(g) = 2.0\text{-}5.5$, $[\text{M}/\text{H}] = -1.0\text{-}+2.0$, and $\text{C}/\text{O} = 0.5\text{-}2.5$ (relative to solar, where solar = 0.458). The models include both equilibrium and disequilibrium chemistry with vertical mixing parameters of $K_{zz} = 10^2\text{-}10^9$ $\text{cm}^2 \text{ s}^{-1}$. While the equilibrium chemistry models have always included rainout processes, the disequilibrium models in Sonora Elf Owl did not, as the abundances of quenched species were

¹² <https://stpsf.readthedocs.io/en/latest/>

Table 2. Photometric measurements of Eps Ind Ab in the JWST/MIRI coronagraphic filters.

| | F1065C | F1140C | F1550C |
|---------------------------------------|------------|------------|------------|
| Flux method 1: <code>spaceKlip</code> | 5.26±0.07 | 8.75±0.10 | 6.69±0.03 |
| Flux method 2: <code>STPSF</code> | 5.06±0.06 | 9.98±0.05 | 7.50±0.002 |
| Flux method 3: TA contrast | 4.96±0.06 | 8.50±0.05 | 6.22±0.001 |
| Adopted Flux | 5.09±0.12 | 9.08±0.64 | 6.80±0.52 |
| Apparent Magnitude [mag] | 13.13±0.03 | 12.21±0.08 | 11.16±0.08 |
| Absolute Magnitude [mag] | 15.33±0.03 | 14.40±0.08 | 13.36±0.08 |

NOTE—All listed fluxes are in units of $10^{-18}\text{W/m}^2/\mu\text{m}$. The adopted fluxes and corresponding uncertainties are the mean and standard deviation of the color measured with each method (see Section 3.1 for details).

held constant above the quench point. For colder atmospheres, however, volatile species such as H_2O , CH_4 , and NH_3 are expected to condense and rain out. In Sonora Flame Skimmer, we adopt a hybrid treatment of disequilibrium chemistry in which these species continue to follow their saturation vapor pressure curves above the quench point. Sonora Flame Skimmer also incorporates the improved CO_2 chemistry treatment introduced in Sonora Elf Owl v2 (N. F. Wogan et al. 2025).

The CMDs are constructed based on the JWST coronagraphic filters, as well as the L’ filter (at $3.8\mu\text{m}$, where Eps Ind Ab has not been detected but for which there is a deep upper limit on the exoplanet flux based on NaCo observations, G. Viswanath et al. 2021). We also show observational data for other cold exoplanets and brown dwarfs, with details on how these were selected and relevant references listed in Appendix A. Warm substellar objects (absolute F1065C magnitude $\gtrsim 10$, corresponding to temperature $\gtrsim 1500\text{K}$) have an F1065C-F1140C color close to 0. Below this temperature, objects are increasingly red in F1065C-F1140C color, due to an increasingly deep ammonia absorption feature. GJ504b, with its F1065C-F1140C color of $0.45 \pm 0.14\text{mag}$, is the only planet to date where a detection of ammonia has been claimed based on MIRI photometric observations; Eps Ind Ab is significantly redder than GJ504b in these filters with a color of $0.88 \pm 0.08\text{mag}$.

Eps Ind Ab is bluer than the “default” models predict at this temperature, and bluer than all of the models presented in E. C. Matthews et al. (2024) in F1065C-F1140C color. Strikingly, the cold brown dwarf WISE 0855 ($\sim 285\text{K}$, K. L. Luhman 2014; H. Kühnle et al. 2025) has almost the same F1065C-F1140C color as Eps Ind Ab, and indeed H. Kühnle et al. (2025) found the ammonia abundance of WISE 0855 to be less than expected from chemical equilibrium modelling, based on their retrieval analysis. In other words, both of these very cold objects show shallower ammonia features than expected, while all of the warmer brown dwarfs shown in

Figure 3 are in broad agreement with the models. The consistency in F1065C-F1140C color of Eps Ind Ab and WISE 0855 suggests that this shallower ammonia feature is typical of very cold atmospheres. The physical mechanism producing this shallower-than-expected ammonia feature is not yet clear, so we now explore several possible scenarios.

A small ammonia feature could indicate a low metallicity for Eps Ind Ab: in this scenario, molecular abundances in the atmosphere would be lower, and their absorption features would be suppressed. The host star Eps Ind A has a slightly sub-solar metallicity (-0.06 ± 0.08 N. C. Santos et al. 2004), and in a gravitational instability formation pathway this could have been inherited by the planet. Metal-poor Sonora Flame Skimmer models with $[\text{M}/\text{H}] = -1.0$ show a good match to the F1065C-F1140C color of Eps Ind Ab (see Figure 4). However, this explanation for the shallow ammonia feature is unsatisfactory: at low metallicity models predict an increased near-IR ($3\text{--}5\mu\text{m}$) brightness for the planet, since there is less atmospheric absorption from molecules such as CO , CO_2 and H_2O . This is inconsistent with archival non-detections of Eps Ind Ab at these wavelengths (M. Janson et al. 2009; G. Viswanath et al. 2021), and indeed E. C. Matthews et al. (2024) argued that Eps Ind Ab likely has an *elevated* metallicity based on its $3\text{--}5\mu\text{m}$ faintness.

We also explored the impact of the vertical mixing (parameterized with the eddy diffusion coefficient, K_{zz}). We tested values between $K_{zz} = 10^2\text{cm}^2/\text{s}$ to $K_{zz} = 10^9\text{cm}^2/\text{s}$, but found that the vertical mixing has no impact on the F1065C-F1140C color in our models, and thus cannot be responsible for suppressing the ammonia feature.

Another explanation to consider for the small ammonia feature is that nitrogen alone is depleted in the exoplanet atmosphere (Figure 5). To test this idea we generated a version of the Sonora Flame Skimmer models with nitrogen depletion but otherwise identical to the

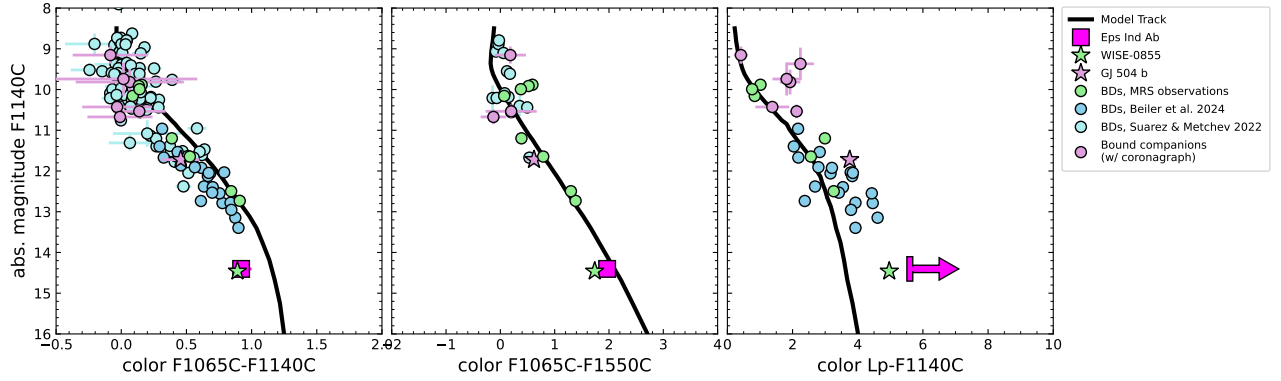


Figure 3. CMD positions of Eps Ind Ab, as well as a number of other cold brown dwarfs (with details provided in Section A), considering the three JWST filters as well as the NaCo L' filter (for which there is a non-detection of Eps Ind Ab; the base of the arrow is the 5σ lower limit in L'-F1065C color for this planet). Models are from the Sonora Flame Skimmer grid (Mang et al. in prep.), and have solar metallicity and C/O and $K_{zz} = 10^7 \text{ cm}^2/\text{s}$. These models broadly explain the population of warmer brown dwarfs, and in particular the trend whereby the F1065C-F1140C color becomes increasingly red, tracing an increasingly deep ammonia feature, in cooler brown dwarfs. However, both Eps Ind Ab and WISE 0855 show significantly bluer F1065C-F1140C colors than these simple models, indicating that the ammonia feature is smaller than expected. Eps Ind Ab and WISE 0855 have remarkably similar mid-IR magnitudes and colors, but Eps Ind Ab is significantly redder in L'-F1065C (i.e., it is significantly fainter at L'), and we discuss potential explanations in the text.

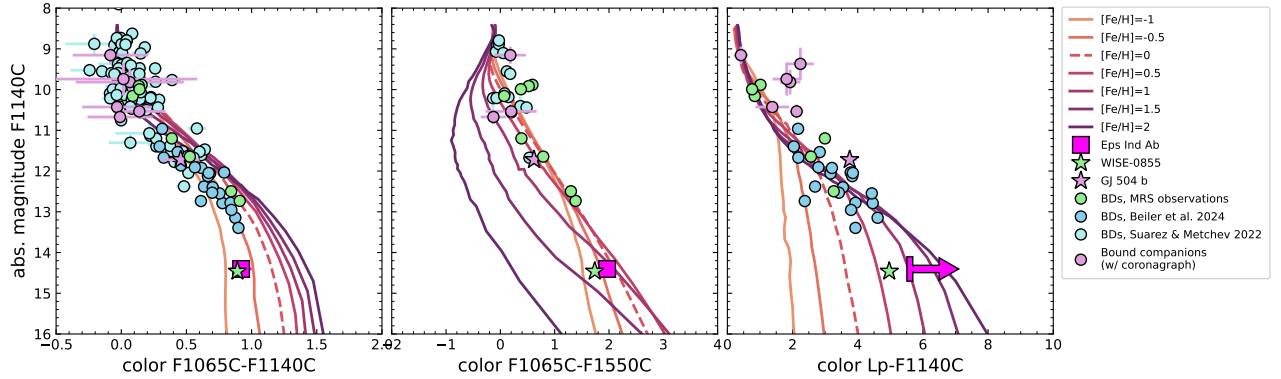


Figure 4. Same as Figure 3, but for models with a range of metallicities. While a significantly sub-solar metallicity would explain the shallow ammonia feature of Eps Ind Ab (left), the models with the lowest metallicity have the brightest NaCo L' magnitude. Sub-solar metallicity is not (by itself) sufficient to explain the in-hand photometric constraints for Eps Ind Ab. All plotted metals have solar C/O and $K_{zz} = 10^7 \text{ cm}^2/\text{s}$, and the model with $[\text{Fe}/\text{H}]=0$ (identical to Figure 3) is highlighted with a dashed line.

default grid models. In Figure 5 we show these models, with either solar metallicity and C/O or the elevated metallicity and C/O inferred by E. C. Matthews et al. (2024). An atmosphere with $\sim 5 - 15\%$ of the equilibrium nitrogen abundance (a depletion of $\sim 85 - 95\%$ of the nitrogen) shows close agreement with the measured F1065C-F1140C color. Removing nitrogen from the atmosphere also increases the L'-F1065C color in these models, and therefore may provide an explanation for the archival non-detections of Eps Ind Ab in the 3-

$5\mu\text{m}$ range (M. Janson et al. 2009; G. Viswanath et al. 2021), though we note that nitrogen depletion alone is not sufficient to explain the Eps Ind Ab L' upper limit and some enrichment of C/O and metallicity is also required. Nonetheless, Figure 5 demonstrates that with significant nitrogen depletion, and with fine-tuning of the carbon and oxygen atom fractions in a cold atmosphere, the CMD positions of both Eps Ind Ab and WISE 0855 can be explained.

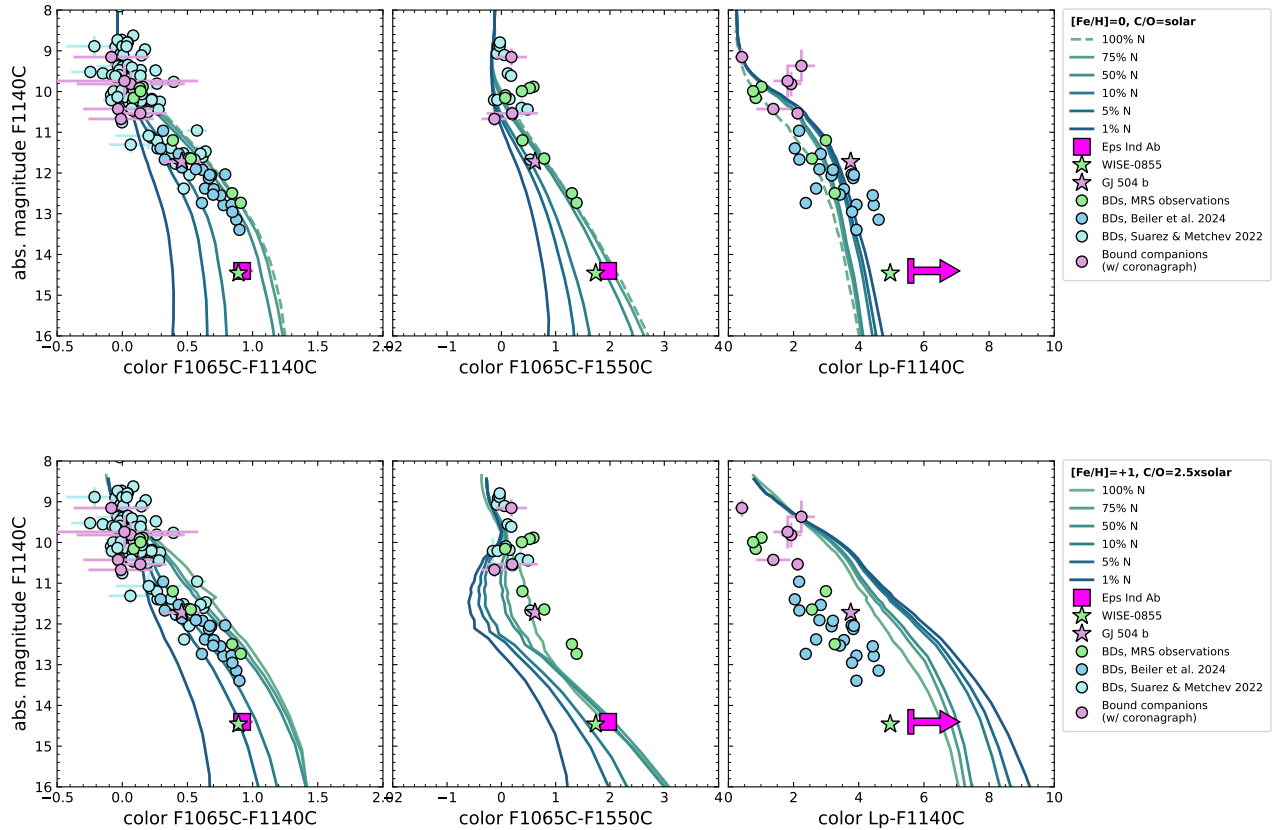


Figure 5. Same as Figure 3, but for models depleted in nitrogen. The top and bottom rows show respectively the case of solar metallicity and C/O, and of enhanced metallicity and C/O as found for Eps Ind Ab in *E. C. Matthews et al. 2024*. Percentage labels indicate the nitrogen content of each atmosphere as a fraction of equilibrium models, and the model from Fig. 3 is highlighted with a dashed line. Atmospheres strongly depleted (to 5%) in nitrogen are consistent with both the F1065C-F1140C color of Eps Ind Ab and WISE 0855, and strongly N-depleted atmospheres also have bluer L'-F1065C colors. However, only in models with *both* (1) depleted nitrogen and (2) enhanced metallicity and C/O is the L'-F1065C color sufficiently blue to match the observational constraints for Eps Ind Ab.

With this in mind, we briefly consider possible explanations for an atmosphere that is depleted in nitrogen (but not carbon or oxygen). There are two explanations worth considering: perhaps this is a signature of formation in a disk, or perhaps nitrogen is actively being removed from the atmosphere through cloud formation and/or rain-out processes. However, neither is a perfect explanation for our observations. Considering the first, it is commonly thought that the formation mechanism and location of a planet within its disk should impact its composition (e.g. *K. I. Öberg et al. 2011*), and *D. Turrini et al. (2021)* modeled the impact of formation location on nitrogen content of the atmosphere. That work found that some formation pathways can lead to planets depleted in nitrogen, but none of their scenarios had depletion as strong as we infer for Eps Ind Ab (85-95%). Further, this formation hypothesis would only apply in the case of WISE 0855 if that brown dwarf

is in fact an ejected planet. The second possibility is that nitrogen atoms are removed from the atmosphere through the formation of clouds. Ammonia-ice clouds are expected to form in very cold atmospheres (e.g. *D. Sudarsky et al. 2000, 2003*); these are also observed in Jupiter (e.g. *P. G. J. Irwin et al. 1998*). However, in our model with water clouds, NH_3 never reaches the pressure-temperature regime required for NH_3 to condense. We note that the pressure-temperature profile for a model without water clouds does cross the NH_3 condensation line (see Appendix B), but there is no reason to expect that such cold atmospheres could appear without water-ice clouds. Another cloud species that may contribute to the nitrogen depletion is ammonium hydrosulfide (NH_4SH ; *C. Visscher et al. 2006*). This cloud forms between the NH_3 and H_2O cloud decks through a reaction between NH_3 and H_2S , and is observed in Jupiter (*P. G. J. Irwin et al. 1998*). However, its for-

mation is limited by the abundance of H_2S , which is expected to be on the order 4 times less abundant than NH_3 , and therefore cannot independently account for the amount of nitrogen that would need to be depleted to explain the Eps Ind Ab color. The final possible avenue for nitrogen depletion is the dissolution of NH_3 into H_2O clouds to form a mixed solution. This process has been investigated in the context of NH_3 depletion in Jupiter (T. Guillot et al. 2020a,b), where vigorous mixing of H_2O ice particles into higher altitudes could allow the NH_3 to dissolve and produce an aqueous solution. Further modeling is necessary to evaluate the effects of this mechanism in colder exoplanetary atmospheres, and future works should also search for absorption signatures of these various cloud species in the Eps Ind Ab atmosphere: NH_3 clouds, in particular, should have several strong features in the near- and mid-IR (J. V. Martonchik et al. 1984).

Finally, we turn to our preferred explanation for the small ammonia feature: perhaps this indicates thick water-ice clouds in the Eps Ind Ab atmosphere. Such clouds could have the dual impacts of (1) reducing the depth of the ammonia feature, thereby producing a bluer F1065C-F1140C color and (2) suppressing the near- and mid-IR emission of the exoplanet, consistent with archival non-detections of this object from the ground between 3 to $5\mu\text{m}$ (M. Janson et al. 2009; G. Viswanath et al. 2021). To test this, we generated a mini-grid of custom models with PICASO (N. E. Batalha et al. 2019; S. Mukherjee et al. 2023; J. Mang et al. 2026) that self-consistently treat clouds using Virga (N. Batalha et al. 2020; N. E. Batalha et al. 2025; S. E. Moran et al. 2025), a Python-based implementation of the A. S. Ackerman & M. S. Marley (2001) cloud model. This grid spans $T_{\text{eff}} = [250, 275, 300 \text{ K}]$, $\log(g) = [4.0, 4.25, 4.5, 4.75]$ (cgs), $[\text{M}/\text{H}] = [0, +0.5, +1.0]$, and $\text{C}/\text{O} = [1.0, 2.5]$. For the disequilibrium models, we parametrize the strength of vertical mixing using an eddy diffusion coefficient of $K_{\text{zz}} = [10^2, 10^9] \text{ cm}^2/\text{s}$. H_2O clouds are parameterized by the sedimentation efficiency parameter, f_{sed} , where larger values produce optically thinner, vertically constrained clouds with large particles, and smaller f_{sed} values result in optically thicker, more vertically extended clouds with smaller particles. In Figure 6 (upper) we demonstrate the effect of introducing water-ice clouds into a model atmosphere, at each of the tested temperatures, using a model with elevated metallicity and C/O as a baseline. Water-ice clouds have more impact at colder temperatures, and produce the expected bluer F1065C-F1140C and redder Lp-1140C colors. We also show an example of a custom PICASO model that includes H_2O clouds self-consistently, as well as a simi-

lar model without water-ice clouds, in Figure 6 (lower). This is the best-fit spectrum from our grid, and is a 275 K object with $\log g = 4.5$, $3\times$ solar metallicity, $2.5\times$ solar C/O, $K_{\text{zz}} = 10^9 \text{ cm}^2/\text{s}$, and $f_{\text{sed}} = 6$. The model contains a highly optically thick H_2O cloud with a column optical depth of 416, reaching $\tau = 1$ near 0.7 bar. Atmospheric models including water-ice clouds can explain the colors of Eps Ind Ab: the model matches the three JWST photometric points, and suppresses the NaCo L' flux of Eps Ind Ab to below the NaCo upper limit (G. Viswanath et al. 2021, but we use the recalculated NaCo upper limit from E. C. Matthews et al. 2024 for Figure 6). Customized cloud models for both Eps Ind Ab and WISE 0855 could explain why both objects have suppressed ammonia features but one is fainter than the other in the 3- $5\mu\text{m}$ region: for example, perhaps Eps Ind Ab has uniform cloud cover while WISE 0855 has only patchy water-ice clouds with holes allowing the near-IR flux to escape, or both objects have similar water-ice clouds but different underlying metallicities and/or carbon-to-oxygen ratios.

While a model atmosphere with water-ice clouds, elevated metallicity, and elevated C/O ratio can explain all in-hand photometry, questions remain. Water-ice clouds are naturally expected in this cold atmosphere, but the elevated metallicity and C/O of our best-fit remains a challenge for formation models. Future studies that expand the wavelength coverage of Eps Ind Ab could more definitively confirm whether or not there are water-ice clouds in this atmosphere, and in particular spectroscopic measurements could provide a more precise measure of the metallicity and C/O ratio, which would be valuable for studying the formation of this cold giant planet, and the cloud f_{sed} , which would be valuable in further constraining the onset of water-ice clouds in cold atmospheres and their typical properties.

5. CONFIRMATION OF COMMON PROPER MOTION

The most definitive evidence that a point source is a planet – and not a background star or galaxy – is the detection of common proper motion between the star and the point source. The significant proper motion of Eps Ind A makes confirming proper motion trivial with more than one epoch of observations: as one of the closest stars to us, Eps Ind A has a proper motion of 4708 mas/year (Gaia Collaboration et al. 2021). Thus, our F1140C re-detection of a point source in the NW quadrant trivially confirms common proper motion between the host star and the point source: a background object would be displaced by [7.57, -4.62] arcsec ([68.8, 42.0] pixels) between the 2023 and 2025 JWST observa-

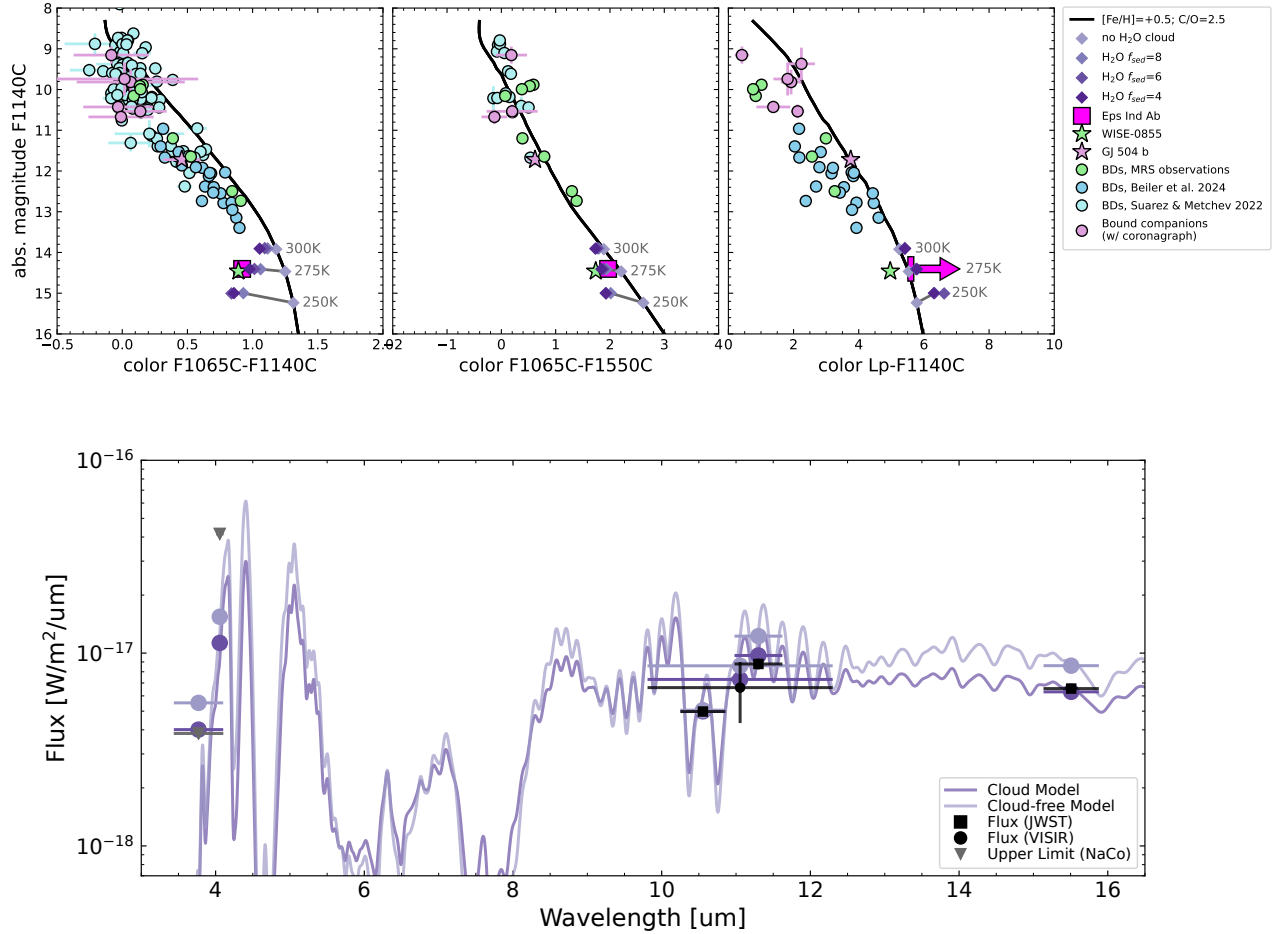


Figure 6. Upper panel: CMD as in Fig. 3, but with the impact of clouds highlighted. The black line shows the trend for the best-fit $[\text{Fe}/\text{H}]$ and C/O from our small grid (see text), while the purple diamonds show the impact of introducing increasingly thick water-ice clouds (parametrized via f_{sed}), for models with temperatures 250 K, 275 K and 300 K. Clouds have a more dramatic impact on the photometry at lower temperatures where they reduce the relative depth of the ammonia feature, making the F1065C-F1140C and F1065C-F1550C colors redder, and subdue the near-IR emission, making the Lp-F1140C color redder.

Lower panel: Model emission spectrum for an atmosphere with thick water-ice clouds, generated with PICASO (N. E. Batalha et al. 2019; S. Mukherjee et al. 2023; J. Mang et al. 2026), and described in detail in the text. We also show a model without water-ice clouds but otherwise identical for reference. The water-ice cloud model is a best-fit from a small grid of models, and is compatible with all in-hand photometry and upper limits for Eps Ind Ab.

tions of the system, inconsistent with our re-detection of the planet in the NE quadrant of the 2025 images. E. C. Matthews et al. (2024) previously argued that Eps Ind Ab was a planet, based in part on archival VISIR/NEAR data collected in 2019 (see also P. Pathak et al. 2021). That dataset showed a detection of a point source with signal-to-noise ~ 3 in the upper left quadrant, consistent with the much more robust point source detection in the 2023 JWST observations. The current dataset (2025 JWST observations) provides the second epoch of observations with $> 5\sigma$ detection significance, and the third detection at any significance of the companion. This result is a definitive demonstration that

the planet shares common proper motion with its host star, and as a consequence also confirms the conclusion of E. C. Matthews et al. (2024) that the low-significance VISIR detection corresponds to the same point source as the JWST detection.

6. UPDATED ORBIT FITS

With our new image astrometry in hand, we re-fit the orbit of Eps Ind Ab and derive an updated dynamical mass. For this orbit fit we follow largely the same method as described in E. C. Matthews et al. (2024), with a few key changes. Similar to that work we used *orvara* (T. D. Brandt et al. 2021) to fit (1) the di-

rect imaging astrometry from this work and from E. C. Matthews et al. (2024); (2) the Hipparcos-Gaia acceleration (also referred to as the Proper Motion Anomaly) of the host star (T. D. Brandt 2018; P. Kervella et al. 2019), using the acceleration derived in the T. D. Brandt (2021) catalog which updates T. D. Brandt (2018) with the inclusion of *Gaia* EDR3 data; (3) RV data from the CES long camera and very long camera (LC and VLC respectively; M. Zechmeister et al. 2013), from UVES (F. Feng et al. 2025), and from HARPS using the data reduction presented in T. Trifonov et al. (2020) and split into three separate regimes where different instrument offsets are expected (referred to as HARPSpre, HARPSpost and HARPSpost2 in F. Feng et al. 2019). The changes in our orbit fitting setup relative to E. C. Matthews et al. (2024) are as follows:

- We use one additional direct imaging astrometry point, derived from the new JWST data presented in this work. The planet has separation 3.654 ± 0.018 arcsec and position angle $35.065 \pm 0.036^\circ$ as measured with JWST on 2025-05-10.
- We correct the LC and VLC radial velocity data for perspective/secular acceleration, as also described in F. Feng et al. (2025). This effect describes the change in the measured radial velocity of a target, due to our changing viewing angle as the target moves across the sky (as opposed to an inherent change in intrinsic velocity of the target), and is particularly relevant for the highest proper-motion stars in the sky, such as Eps Ind A (M. Kürster et al. 2003). Note that for HARPS and UVES, published data already include a perspective acceleration correction, while for LC and VLC the published data do not include this correction.
- We apply a nightly binning to all datasets, whereas E. C. Matthews et al. (2024) applied nightly binning only to the HARPS data. Thus, our fit includes 266 independent RV points, with 202 from HARPS, 44 from LC, 17 from VLC, and 3 from UVES. For nights with 3 or fewer measurements from a single instrument we combined RV uncertainties in quadrature, while for nights with more than 3 measurements we took the standard deviation of the unbinned RV measurements as the RV uncertainty.

The on-sky orbit and evolution of separation and position angle of the planet relative to its host star are shown in Figure 7 for our best-fit orbit. In Appendix D we include a corner plot of key orbital parameters that highlights the correlations of these parameters and the

impact on the orbit fit of the newest astrometric point derived in this work.

We find a more massive planet ($7.63_{-0.70}^{+0.73} M_{\text{Jup}}$) than E. C. Matthews et al. (2024) with this set-up, with a smaller semi-major axis ($20.9_{-3.3}^{+5.8}$ AU) and a lower eccentricity ($0.244_{-0.083}^{+0.11}$). This change is driven primarily by the corrected perspective acceleration treatment of the RV data, and the updated binning of the RV points, rather than the additional image astrometry point (see Appendix D and F. Feng et al. 2025). The best-fit orbit explains all available RV, astrometric and direct imaging datasets; our mass shows good agreement with the findings of F. Feng et al. (2025) but we find an orbital period that is $\sim 1.2\sigma$ lower than in F. Feng et al. (2025) and an eccentricity that is $\sim 1.9\sigma$ lower than in F. Feng et al. (2025). The semi-major axis and eccentricity are strongly correlated for an orbit with incomplete phase coverage; Eps Ind Ab is in this regime with ~ 30 years of RV data and a best-fit period of ~ 110 years. Thus, it is unsurprising that both the semi-major axis and eccentricity diverge in the same direction from the values of F. Feng et al. (2025). Note also that with the orbit fit in this work, orbits close to circular are compatible with the data, and would have semi-major axis ~ 19 au.

Considering the on-sky orbit of Eps Ind Ab, the new astrometric point provides a significant improvement in the inclination constraint: the precision is doubled, and the derived value is $\sim 1.3\sigma$ lower than for a fit without the new astrometry included. This is unsurprising, given that we now have two precise astrometric measurements of the planet with JWST; the updated inclination also has a small impact on the derived mass (since the radial velocity data is sensitive to the $m \sin i$ of the planet, which changes by $\sim 2\%$ in the fit with two JWST epochs vs the fit without). Ongoing monitoring of the radial velocity and relative astrometry in this system will remain important for refining the orbital solutions, and in particular, sufficiently long-term monitoring will help to break the degeneracy between eccentricity and semi-major axis (Rajpoot et al. in prep.).

7. DISCUSSION & CONCLUSIONS

In this work we have presented new coronagraphic observations of the Eps Ind A system, collected at $11.3\mu\text{m}$ during the 2nd JWST epoch for this target. Combining the new and archival data, we make the following key conclusions:

- We find photometric evidence for the presence of ammonia in the planet Eps Ind Ab, with a shallower absorption feature than expected (F1065C-F1140C= 0.88 ± 0.08 mag). This could imply a low-metallicity planet (a conclusion which is in ten-

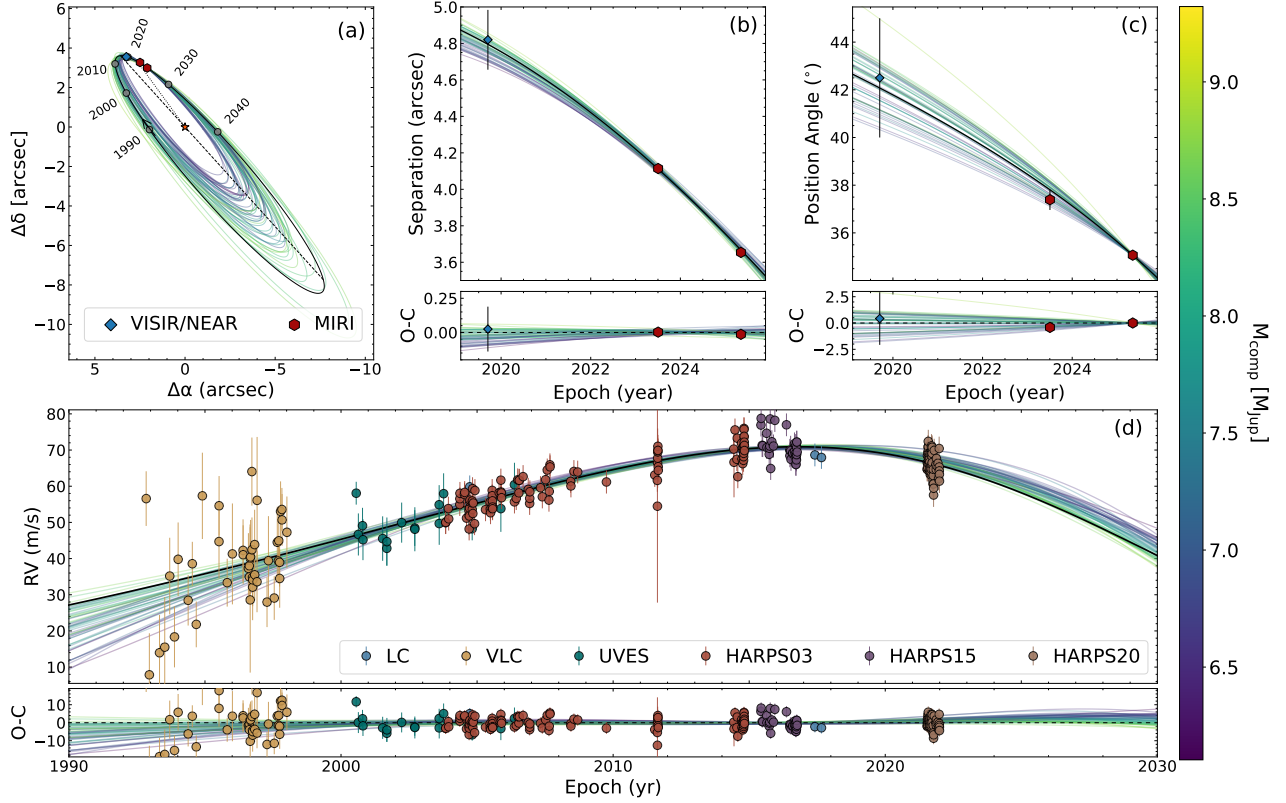


Figure 7. Best-fit orbit solutions. Here we show the on-sky orbit traced by Eps Ind Ab in panel (a); the evolution of on-sky separation and position angle of the planet during our observational baseline in panels (b) and (c) respectively; and the RV data in panel (d). The Maximum A Posteriori (MAP) solution is shown with a thick black line, alongside 50 randomly drawn samples from the posterior, with the same colorbar applying to all panels. Our measured JWST/MIRI and VISIR/NEAR astrometry is shown with red hexagons and a blue diamond respectively, and the predicted on-sky orbit position of the exoplanet between 1990-2040 is indicated with small grey points.

sion with the L' non-detection of the planet), or a strongly depleted nitrogen abundance in the atmosphere. However, our preferred explanation is that this indicates the presence of water-ice clouds in the exoplanet atmosphere. Even with clouds, the photometry still suggests an elevated C/O and metallicity for Eps Ind Ab, which remains a challenge for formation models.

- We present updated orbit fits for the companion Eps Ind Ab, with a somewhat higher mass ($7.6 \pm 0.7 M_{\text{Jup}}$) and lower eccentricity ($0.24^{+0.11}_{-0.08}$) than were derived in [E. C. Matthews et al. \(2024\)](#). This change in orbital parameters is largely driven by an updated treatment of the radial velocities, though the new JWST imaging point is particularly helpful in refining the on-sky inclination of the orbit.
- We strongly confirm that Eps Ind Ab shares common proper motion with its host star (as already inferred in [E. C. Matthews et al. 2024](#)) with the

third detection epoch (and the second at $> 5\sigma$) of the companion.

Eps Ind Ab joins a small but growing population of exoplanets with observed ammonia, namely the directly imaged GJ 504 b ([M. Mâlin et al. 2025](#)), and possibly the transiting WASP-107b ([L. Welbanks et al. 2024](#)) and the directly imaged 51 Eri b ([N. Whiteford et al. 2023](#)). Eps Ind Ab is the coldest planet with an ammonia detection to date. Eps Ind Ab and WISE 0855 are the only two substellar objects that both (1) have ammonia detections and (2) are also cold enough for water- and possibly nitrogen-containing cloud species to potentially condense in their atmospheres. Both have a shallow ammonia feature, raising an important open question about the physics driving this ammonia suppression that should be investigated further. Upcoming photometric and spectroscopic JWST observations of Eps Ind Ab between $3\text{-}20\mu\text{m}$ (GO #8438, [O. Berne et al. 2025](#) and #8714, [J. Xuan et al. 2025](#)) will provide an increasingly detailed look at this cold atmosphere, and in particular

Table 3. Best-fit parameters for the orbit of Eps Ind Ab, listed with 1σ uncertainties.

| Parameter | Median Posterior | Prior |
|---------------------------------------|-----------------------------|---|
| <i>Fitted Parameters</i> | | |
| $M_{\text{host}}[M_{\odot}]$ | $0.781^{+0.036}_{-0.037}$ | $0.76 \pm 0.04 M_{\odot}$ (Gaussian) |
| $M_{\text{comp}}[M_{\text{Jup}}]$ | $7.63^{+0.73}_{-0.70}$ | $1/M_{\text{comp}}$ |
| a [AU] | $20.9^{+5.8}_{-3.3}$ | $1/a$ |
| $\sqrt{e} \sin \omega$ | $0.383^{+0.079}_{-0.10}$ | Uniform |
| $\sqrt{e} \cos \omega$ | $0.22^{+0.25}_{-0.36}$ | Uniform |
| i [°] | $102.3^{+1.9}_{-1.7}$ | $\sin(i)$, $0^{\circ} < i < 180^{\circ}$ |
| Ω [°] | $44.6^{+1.3}_{-1.3}$ | Uniform |
| λ_{ref} [°] | $356.1^{+8.6}_{-9.8}$ | Uniform |
| Parallax (mas) | $274.844^{+0.015}_{-0.015}$ | 274.84 ± 0.096 mas (Gaussian) |
| RV Jitter σ_{jit} [m/s] | $3.23^{+0.17}_{-0.16}$ | $1/\sigma_{\text{jit}}$, $\sigma_{\text{jit}} \in (0, 1000]$ m/s |
| <i>Derived Parameters</i> | | |
| P (yr) | 108^{+49}_{-25} | ... |
| e | $0.244^{+0.11}_{-0.083}$ | ... |
| ω [°] | 62^{+48}_{-27} | ... |
| a [arcsec] | $5.7^{+1.6}_{-0.9}$ | ... |

NOTE—Priors for stellar mass prior and parallax are based on B.-O. Demory et al. (2009) and Gaia Collaboration et al. (2023) respectively.

should provide a clearer answer for why the ammonia feature in Eps Ind Ab is shallower than models predict, and may confirm whether its atmosphere contains thick water-ice clouds.

Increasing the sample of cold exoplanets with photometric and/or spectroscopic data in the upcoming years will provide more insight into the key physics of these cold atmospheres. In particular, it would be highly valuable to measure F1065C and F1140C photometry of other extremely cold exoplanets and brown dwarfs, and determine whether these have similarly shallow ammonia features as Eps Ind Ab and WISE 0855 and when the ammonia feature starts to diverge from model predictions. Since the discovery of Eps Ind Ab, two other cold exoplanets have been imaged with JWST: 14 Her c (D. C. Bardalez Gagliuffi et al. 2025) and TWA 7 b (A. M. Lagrange et al. 2025; K. A. Crotts et al. 2025); MIRI multi-band photometry of both objects would be highly valuable in confirming the depth of their ammonia features. Strikingly, both of these exoplanets have fainter-than-expected $4.4\mu\text{m}$ magnitudes, based on NIRCcam coronagraphic observations; Eps Ind Ab

has no published NIRCcam observations but NaCo non-detections confirm that this planet is also fainter than expected in the $3\text{--}5\mu\text{m}$ wavelength range. Together, this sample of cold planets is painting a consistent picture: cold planets are very faint between $3\text{--}5\mu\text{m}$, which may be due to the presence of water-ice clouds, and this is an important consideration when designing future photometric searches for cold exoplanets.

ACKNOWLEDGMENTS

We thank Ewan Douglas, Dominique Petit dit de la Roche, and Florian Philipot for their contributions to the proposal on which this work is based. We also thank the anonymous referee for a thorough report which has certainly improved the quality of the paper.

This work is based on observations made with the NASA/ESA/CSA James Webb Space Telescope. The data were obtained from the Mikulski Archive for Space Telescopes at the Space Telescope Science Institute, which is operated by the Association of Universities for Research in Astronomy, Inc., under NASA contract NAS

5-03127 for JWST. These observations are associated with program #5037 and #2243, of which support was provided by NASA through a grant from the Space Telescope Science Institute, which is operated by the Association of Universities for Research in Astronomy, Inc., under NASA contract NAS 5-03127.

J.M. acknowledges support from the National Science Foundation Graduate Research Fellowship Program under Grant No. DGE 2137420. L.A.B. acknowledges support from the Dutch Research Council (NWO) under grant VI.Veni.242.055 (<https://doi.org/10.61686/LAJVP77714>). J.A.B. acknowledges that part of this research was carried out at the Jet Propulsion Laboratory, California Institute of Technology, under contract with the National Aeronautics and Space Administration (NASA).

AUTHOR CONTRIBUTIONS

ECM designed the project and led the observational design, data analysis and interpretation for this paper, and wrote the manuscript. ECM also led the observing proposal upon which this paper is based, with support

from LB, JAB, ALC, IJMC, ED, FF, AML, CVM, FP and MWP. JM provided cold model atmospheres and color-magnitude diagram data, as well as contributions to the interpretation and text for Section 4, with support from CM. MM and ALC contributed to the data reduction. BR contributed to the orbit fitting analysis. Finally, all authors read the manuscript and provided comments.

Facilities: JWST (MIRI)

Software: `spaceKLIP` (J. Kammerer et al. 2022; A. L. Carter et al. 2023), `STPSF` (M. D. Perrin et al. 2014), `PICASO` (N. E. Batalha et al. 2019; S. Mukherjee et al. 2023; J. Mang et al. 2026), `Virga` (N. Batalha et al. 2020; N. E. Batalha et al. 2025; S. E. Moran et al. 2025), `astropy` (Astropy Collaboration et al. 2013, 2018, 2022), `scipy` (P. Virtanen et al. 2020), `numpy` (C. R. Harris et al. 2020), `pandas` (W. McKinney 2010; The pandas development team 2021), `matplotlib` (J. D. Hunter 2007), `seaborn` (M. L. Waskom 2021).

APPENDIX

A. ARCHIVAL BROWN DWARF & PLANET PHOTOMETRY

In this Section we provide the references and inclusion criteria for the brown dwarfs and planets shown in Figures 3-5. No brown dwarfs have been observed photometrically with the MIRI coronagraphic filters, but we used spectroscopic observations to generate synthetic photometry of several field brown dwarfs for our CMD. For this we used spectroscopic observations of two main samples of cool brown dwarfs: the archive of ultracool brown dwarfs observed with Spitzer/IRS as assembled in G. Suárez & S. Metchev (2022), and sample of T- and Y-type brown dwarfs observed with JWST/LRS by S. A. Beiler et al. (2024). In order to improve the visual clarity of Figure 3, we restricted the G. Suárez & S. Metchev (2022) sample to targets with a distance precision of 5% or better, while for the S. A. Beiler et al. (2024) sample we included all targets. We calculated photometry and associated uncertainties by integrating these spectra through the relevant JWST filters and through the NaCo L' filter, making the optimistic assumption that uncertainties on individual bins are uncorrelated, and combined all uncertainties in quadrature. Note that not all of these brown dwarfs have spectral coverage across the full relevant wavelength range, and these appear in only a subset of panels in Figure 3.

There are also a handful of MIRI/MRS observations of cold brown dwarfs, which provide the best combination of sensitivity and wavelength coverage for any cold substellar objects, and in particular can be used to calculate synthetic photometry for cold brown dwarfs in the 15.5 μ m MIRI coronagraphic filter. The relevant targets are WISE 0855 (H. Kühnle et al. 2025), WISE 1828 (D. Barrado et al. 2023), WISE 1738 (M. Vasist et al. 2025), WISE 0458 (E. C. Matthews et al. 2025), Ross 458C (Whiteford et al. in prep.), VHS 1256 b (B. E. Miles et al. 2023), PSO J318 (P. Mollière et al. 2025), 2MASS2148 and 2MASS0624 (priv. comm., from program GO #2288, PI Lothringer). In each case, we used the data reductions from the published papers, since there are systematic biases in the MAST data reductions (see Appendix C for details). Where possible, we supplemented these observations with near-IR JWST spectra so as to derive a NaCo L' magnitude. These are available in the same publications as the MRS data for Ross 458C, VHS 1256 b, PSO J318, 2MASS2148 and 2MASS0624, and in dedicated publications for WISE 0855 (K. L. Luhman et al. 2024) and WISE 1828 (B. W. P. Lew et al. 2024).

Figures 3-5 also highlight the CMD positions of bound substellar companions for which both F1065C and F1140C coronagraphic observations are available. We focus only on systems with published observations

in both the F1065C and F1140C MIRI filters, since our primary focus in this analysis is the ammonia feature. There are five other systems (with eight companions) that meet this criterion: HR8799bcde (A. Boccaletti et al. 2023), HD95086b (M. Mâlin et al. 2024), GJ504b (M. Mâlin et al. 2025), HR2562B (N. Godoy et al. 2024) and Kap And b (N. Godoy et al. 2025). We supplemented these data with L' photometry collected from the ground for targets where these are available, namely HR8799bcde (C. Marois et al. 2008, 2010), GJ504b (M. Kuzuhara et al. 2013), HD95086b (J. Rameau et al. 2013) and Kap And b (M. Bonnefoy et al. 2014).

B. H₂O AND NH₃ CONDENSATION

In Figure 8 we provide condensation curves for both H₂O and NH₃, alongside the pressure-temperature (P-T) profile for several atmosphere models. First, we show the custom cloud model from Figure 6; in this scenario H₂O condenses but NH₃ condensation is not expected. Second, we show the best-fit model presented in E. C. Matthews et al. (2024): a model from the Sonora Elf Owl suite (S. Mukherjee et al. 2024), with temperature 275 K, 10× solar metallicity, 2.5× solar C/O, and $K_{zz} = 10^9$ cm²/s. In this scenario H₂O condenses at ~ 0.3 bar, and NH₃ condenses at ~ 0.02 bar, and so both cloud species should be able to form. The production of ammonia clouds in Eps Ind Ab depends finely on the exact atmospheric state, and future works should explore this question in more detail, both observationally and theoretically.

C. BIASES IN MIRI/MRS PRE-REDUCED MAST SPECTRA

We used MIRI/MRS archival spectra of cold brown dwarfs as part of our effort to construct observational CMDs. While compiling this data, we found a significant difference between the CMD positions of pre-reduced spectra acquired directly from MAST and from peer-reviewed papers presenting each individual spectrum. This is demonstrated in Figure 9, where we show an F1065C-F1140C color based on MIRI/MRS observations, as derived from either the MAST data reductions or the published data reductions. The effect is most pronounced for the coldest brown dwarf observations (e.g. WISE0458, WISE1828 and especially WISE1738), likely because these are the faintest brown dwarfs and any systematic effects can therefore bias the spectrum most strongly. Further, we see that MAST data reductions consistently imply a larger F1140C-F1065C color than the published data reductions.

Presumably, this is due to custom data reduction choices made in the more detailed analyses for published

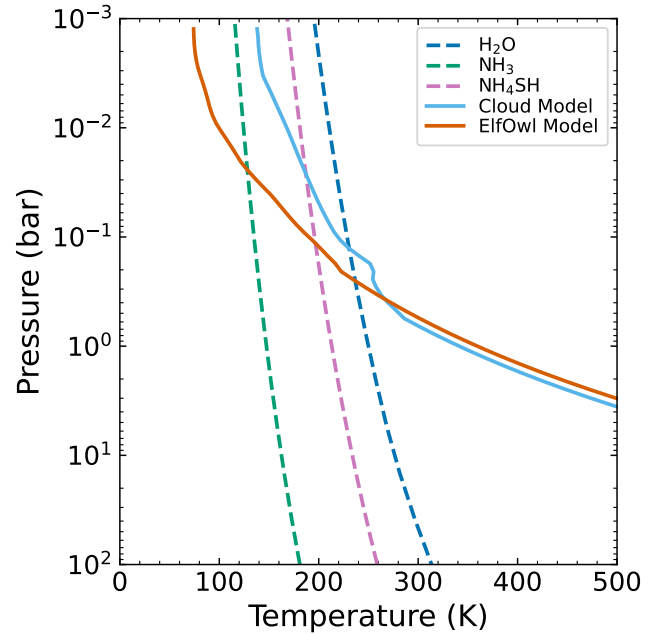


Figure 8. Condensation curves for H₂O, NH₄SH and NH₃, plotted against two pressure-temperature profiles: (1) a 275 K Sonora ElfOwl model with elevated metallicity ([Fe/H]=1.0) and C/O (2.5× solar), for which all three cloud species could form, and (2) our custom cloud model from Figure 6, for which H₂O and NH₄SH but *not* NH₃ clouds are expected to form. The NH₄SH curve is plotted following the equation provided in C. Visscher et al. (2006), for metallicity 3× solar.

papers, such as whether the background is subtracted based on an annulus in the same observation or based on a dithered observation of the target (see e.g. D. Barrado et al. 2023; H. Kühnle et al. 2025), and any custom routines that are used to reduce/remove systematics (e.g. B. E. Miles et al. 2023; E. C. Matthews et al. 2025). By nature, the default MAST reductions are designed to be applicable to as broad a range of observations as possible, and are not customized to specific science cases. This divergence between the MAST spectra and the published spectra serves as a reminder of the need for dedicated data reductions, especially for low signal-to-noise targets, and careful checks to ensure that systematics in the data are understood and removed where possible.

D. CORRELATIONS OF ORBIT FITTING PARAMETERS

In Figure 10 we include a corner plot showing the correlations between key orbit parameters, as derived using `orvara` (T. D. Brandt et al. 2021). We additionally show posteriors without the newest imaging point, to demon-

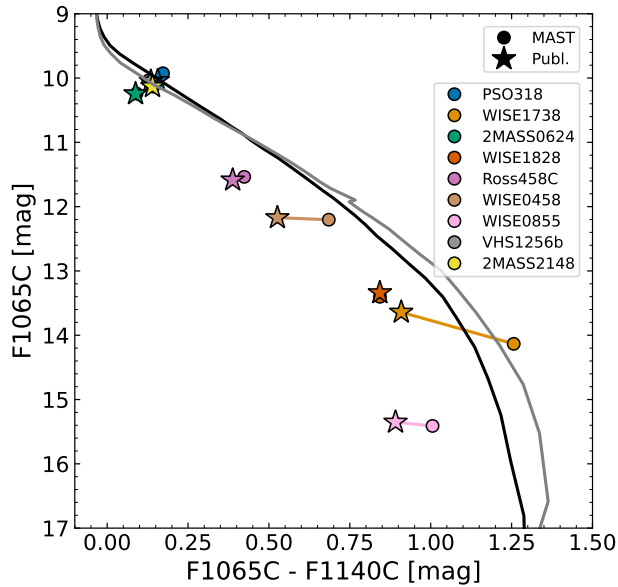


Figure 9. Comparison between CMD positions based on default MAST spectra (circles) and custom data reductions (stars) which are expected to be more reliable for these faint brown dwarfs. This demonstrates the importance of carefully considering systematics when reducing JWST/MRS data. For reference, Sonora Flame Skimmer models with $[\text{Fe}/\text{H}]=0.0$ (black) and 0.5 (grey) are indicated: the biases in MAST spectra are sufficient that they can significantly impact which model is deemed the best fit to JWST data.

strate how this imaging epoch impacts the parameter values.

REFERENCES

- Ackerman, A. S., & Marley, M. S. 2001, *ApJ*, 556, 872, doi: [10.1086/321540](https://doi.org/10.1086/321540)
- Astropy Collaboration, Robitaille, T. P., Tollerud, E. J., et al. 2013, *A&A*, 558, A33, doi: [10.1051/0004-6361/201322068](https://doi.org/10.1051/0004-6361/201322068)
- Astropy Collaboration, Price-Whelan, A. M., Sipőcz, B. M., et al. 2018, *AJ*, 156, 123, doi: [10.3847/1538-3881/aabc4f](https://doi.org/10.3847/1538-3881/aabc4f)
- Astropy Collaboration, Price-Whelan, A. M., Lim, P. L., et al. 2022, *ApJ*, 935, 167, doi: [10.3847/1538-4357/ac7c74](https://doi.org/10.3847/1538-4357/ac7c74)
- Bardalez Gagliuffi, D. C., Balmer, W. O., Pueyo, L., et al. 2025, *ApJL*, 988, L18, doi: [10.3847/2041-8213/ade30f](https://doi.org/10.3847/2041-8213/ade30f)
- Barrado, D., Mollière, P., Patapis, P., et al. 2023, *Nature*, 624, 263, doi: [10.1038/s41586-023-06813-y](https://doi.org/10.1038/s41586-023-06813-y)
- Batalha, N., caoimherooney11, & sagnickm. 2020, natashabatalha/virga: Initial Release, v0.0 Zenodo, doi: [10.5281/zenodo.3759888](https://doi.org/10.5281/zenodo.3759888)
- Batalha, N. E., Marley, M. S., Lewis, N. K., & Fortney, J. J. 2019, *ApJ*, 878, 70, doi: [10.3847/1538-4357/ab1b51](https://doi.org/10.3847/1538-4357/ab1b51)
- Batalha, N. E., Rooney, C. M., Visscher, C., et al. 2025, arXiv e-prints, arXiv:2508.15102, doi: [10.48550/arXiv.2508.15102](https://doi.org/10.48550/arXiv.2508.15102)
- Beiler, S. A., Mukherjee, S., Cushing, M. C., et al. 2024, *ApJ*, 973, 60, doi: [10.3847/1538-4357/ad6759](https://doi.org/10.3847/1538-4357/ad6759)
- Berne, O., Amiot, P., Canin, A., & Schroetter, I. 2025, The first spectrum of a temperate super-Jupiter planet,, JWST Proposal. Cycle 4, ID. #8438
- Boccaletti, A., Lagage, P. O., Baudoz, P., et al. 2015, *PASP*, 127, 633, doi: [10.1086/682256](https://doi.org/10.1086/682256)
- Boccaletti, A., Cossou, C., Baudoz, P., et al. 2022, *A&A*, 667, A165, doi: [10.1051/0004-6361/202244578](https://doi.org/10.1051/0004-6361/202244578)
- Boccaletti, A., Mâlin, M., Baudoz, P., et al. 2023, arXiv e-prints, arXiv:2310.13414, doi: [10.48550/arXiv.2310.13414](https://doi.org/10.48550/arXiv.2310.13414)
- Bonnefoy, M., Currie, T., Marleau, G.-D., et al. 2014, *A&A*, 562, A111, doi: [10.1051/0004-6361/201322119](https://doi.org/10.1051/0004-6361/201322119)
- Bowler, B. P. 2016, *PASP*, 128, 102001, doi: [10.1088/1538-3873/128/968/102001](https://doi.org/10.1088/1538-3873/128/968/102001)

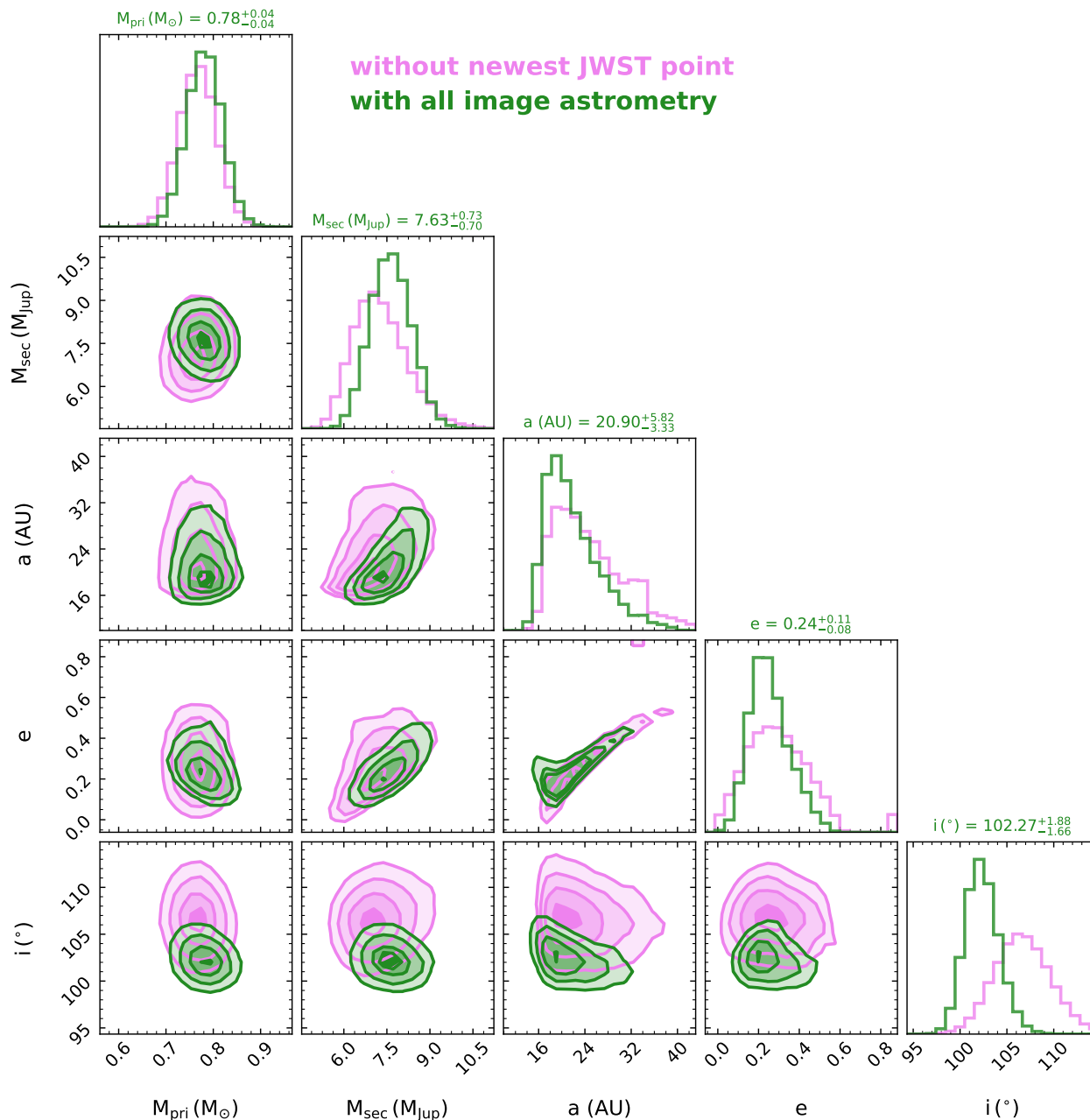


Figure 10. Posterior correlations for key orbit parameters. Green (pink) posteriors show values with (without) the latest JWST point; the orbit fits are otherwise identical. Parameters above each histogram correspond to the best-fit values with the newest JWST image astrometry included.

Brandt, T. D. 2018, *ApJS*, 239, 31,
doi: [10.3847/1538-4365/aaec06](https://doi.org/10.3847/1538-4365/aaec06)

Brandt, T. D. 2021, *ApJS*, 254, 42,
doi: [10.3847/1538-4365/abf93c](https://doi.org/10.3847/1538-4365/abf93c)

Brandt, T. D., Dupuy, T. J., Li, Y., et al. 2021, *AJ*, 162,
186, doi: [10.3847/1538-3881/ac042e](https://doi.org/10.3847/1538-3881/ac042e)

Bushouse, H., Eisenhamer, J., Dencheva, N., et al. 2023,
JWST Calibration Pipeline, 1.12.5 Zenodo,
doi: [10.5281/zenodo.10022973](https://doi.org/10.5281/zenodo.10022973)

Carter, A. L., Hinkley, S., Kammerer, J., et al. 2023, *ApJL*,
951, L20, doi: [10.3847/2041-8213/acd93e](https://doi.org/10.3847/2041-8213/acd93e)

Coles, P. A., Yurchenko, S. N., & Tennyson, J. 2019,
MNRAS, 490, 4638, doi: [10.1093/mnras/stz2778](https://doi.org/10.1093/mnras/stz2778)

Crotts, K. A., Carter, A. L., Lawson, K., et al. 2025, *ApJL*,
987, L41, doi: [10.3847/2041-8213/ade798](https://doi.org/10.3847/2041-8213/ade798)

Cushing, M. C., Kirkpatrick, J. D., Gelino, C. R., et al.
2011, *ApJ*, 743, 50, doi: [10.1088/0004-637X/743/1/50](https://doi.org/10.1088/0004-637X/743/1/50)

- Demory, B.-O., Ségransan, D., Forveille, T., et al. 2009, *A&A*, 505, 205, doi: [10.1051/0004-6361/200911976](https://doi.org/10.1051/0004-6361/200911976)
- Feng, F., Anglada-Escudé, G., Tuomi, M., et al. 2019, *MNRAS*, 490, 5002, doi: [10.1093/mnras/stz2912](https://doi.org/10.1093/mnras/stz2912)
- Feng, F., Xiao, G.-Y., Jones, H. R. A., et al. 2025, *MNRAS*, 539, 3180, doi: [10.1093/mnras/staf689](https://doi.org/10.1093/mnras/staf689)
- Gaia Collaboration, Brown, A. G. A., Vallenari, A., et al. 2021, *A&A*, 649, A1, doi: [10.1051/0004-6361/202039657](https://doi.org/10.1051/0004-6361/202039657)
- Gaia Collaboration, Vallenari, A., Brown, A. G. A., et al. 2023, *A&A*, 674, A1, doi: [10.1051/0004-6361/202243940](https://doi.org/10.1051/0004-6361/202243940)
- Godoy, N., Choquet, E., Serabyn, E., et al. 2024, *A&A*, 689, A185, doi: [10.1051/0004-6361/202449951](https://doi.org/10.1051/0004-6361/202449951)
- Godoy, N., Choquet, E., Serabyn, E., et al. 2025, *A&A*, 702, A4, doi: [10.1051/0004-6361/202554652](https://doi.org/10.1051/0004-6361/202554652)
- Green, J. J., Beichman, C., Basinger, S. A., et al. 2005, in *Society of Photo-Optical Instrumentation Engineers (SPIE) Conference Series*, Vol. 5905, *Techniques and Instrumentation for Detection of Exoplanets II*, ed. D. R. Coulter, 185–195, doi: [10.1117/12.619343](https://doi.org/10.1117/12.619343)
- Guillot, T., Stevenson, D. J., Atreya, S. K., Bolton, S. J., & Becker, H. N. 2020a, *Journal of Geophysical Research (Planets)*, 125, e06403, doi: [10.1029/2020JE006403](https://doi.org/10.1029/2020JE006403)
- Guillot, T., Li, C., Bolton, S. J., et al. 2020b, *Journal of Geophysical Research (Planets)*, 125, e06404, doi: [10.1029/2020JE006404](https://doi.org/10.1029/2020JE006404)
- Harris, C. R., Millman, K. J., van der Walt, S. J., et al. 2020, *Nature*, 585, 357, doi: [10.1038/s41586-020-2649-2](https://doi.org/10.1038/s41586-020-2649-2)
- Hunter, J. D. 2007, *Computing in Science & Engineering*, 9, 90, doi: [10.1109/MCSE.2007.55](https://doi.org/10.1109/MCSE.2007.55)
- Irwin, P. G. J., Weir, A. L., Smith, S. E., et al. 1998, *J. Geophys. Res.*, 103, 23001, doi: [10.1029/98JE00948](https://doi.org/10.1029/98JE00948)
- Janson, M., Apai, D., Zechmeister, M., et al. 2009, *MNRAS*, 399, 377, doi: [10.1111/j.1365-2966.2009.15285.x](https://doi.org/10.1111/j.1365-2966.2009.15285.x)
- Kammerer, J., Stark, C. C., Ludwick, K. J., Juanola-Parramon, R., & Nemati, B. 2022, *AJ*, 164, 235, doi: [10.3847/1538-3881/ac97eb](https://doi.org/10.3847/1538-3881/ac97eb)
- Kervella, P., Arenou, F., Mignard, F., & Thévenin, F. 2019, *A&A*, 623, A72, doi: [10.1051/0004-6361/201834371](https://doi.org/10.1051/0004-6361/201834371)
- Krist, J. E., Balasubramanian, K., Beichman, C. A., et al. 2009, in *Society of Photo-Optical Instrumentation Engineers (SPIE) Conference Series*, Vol. 7440, *Techniques and Instrumentation for Detection of Exoplanets IV*, ed. S. B. Shaklan, 74400W, doi: [10.1117/12.826448](https://doi.org/10.1117/12.826448)
- Kühnle, H., Patapis, P., Mollière, P., et al. 2025, *A&A*, 695, A224, doi: [10.1051/0004-6361/202452547](https://doi.org/10.1051/0004-6361/202452547)
- Kürster, M., Endl, M., Rouesnel, F., et al. 2003, *A&A*, 403, 1077, doi: [10.1051/0004-6361:20030396](https://doi.org/10.1051/0004-6361:20030396)
- Kuzuhara, M., Tamura, M., Kudo, T., et al. 2013, *ApJ*, 774, 11, doi: [10.1088/0004-637X/774/1/11](https://doi.org/10.1088/0004-637X/774/1/11)
- Lagrange, A. M., Wilkinson, C., Mâlin, M., et al. 2025, *Nature*, 642, 905, doi: [10.1038/s41586-025-09150-4](https://doi.org/10.1038/s41586-025-09150-4)
- Lajoie, C.-P., Soummer, R., Pueyo, L., et al. 2016, in *Society of Photo-Optical Instrumentation Engineers (SPIE) Conference Series*, Vol. 9904, *Space Telescopes and Instrumentation 2016: Optical, Infrared, and Millimeter Wave*, ed. H. A. MacEwen, G. G. Fazio, M. Lystrup, N. Batalha, N. Siegler, & E. C. Tong, 99045K, doi: [10.1117/12.2233032](https://doi.org/10.1117/12.2233032)
- Lew, B. W. P., Roellig, T., Batalha, N. E., et al. 2024, *AJ*, 167, 237, doi: [10.3847/1538-3881/ad3425](https://doi.org/10.3847/1538-3881/ad3425)
- Luhman, K. L. 2014, *ApJL*, 786, L18, doi: [10.1088/2041-8205/786/2/L18](https://doi.org/10.1088/2041-8205/786/2/L18)
- Luhman, K. L., Tremblin, P., Alves de Oliveira, C., et al. 2024, *AJ*, 167, 5, doi: [10.3847/1538-3881/ad0b72](https://doi.org/10.3847/1538-3881/ad0b72)
- Mâlin, M., Boccaletti, A., Perrot, C., et al. 2024, *A&A*, 690, A316, doi: [10.1051/0004-6361/202450470](https://doi.org/10.1051/0004-6361/202450470)
- Mâlin, M., Boccaletti, A., Perrot, C., et al. 2025, *A&A*, 693, A315, doi: [10.1051/0004-6361/202452695](https://doi.org/10.1051/0004-6361/202452695)
- Mang, J., Batalha, N. E., Morley, C. V., et al. 2026, *arXiv e-prints*, arXiv:2602.22468, doi: [10.48550/arXiv.2602.22468](https://doi.org/10.48550/arXiv.2602.22468)
- Marley, M. S., Saumon, D., Visscher, C., et al. 2021, *ApJ*, 920, 85, doi: [10.3847/1538-4357/ac141d](https://doi.org/10.3847/1538-4357/ac141d)
- Marois, C., Macintosh, B., Barman, T., et al. 2008, *Science*, 322, 1348, doi: [10.1126/science.1166585](https://doi.org/10.1126/science.1166585)
- Marois, C., Zuckerman, B., Konopacky, Q. M., Macintosh, B., & Barman, T. 2010, *Nature*, 468, 1080, doi: [10.1038/nature09684](https://doi.org/10.1038/nature09684)
- Martonchik, J. V., Orton, G. S., & Appleby, J. F. 1984, *ApOpt*, 23, 541, doi: [10.1364/AO.23.000541](https://doi.org/10.1364/AO.23.000541)
- Matthews, E. C., Carter, A. L., Pathak, P., et al. 2024, *Nature*, 633, 789, doi: [10.1038/s41586-024-07837-8](https://doi.org/10.1038/s41586-024-07837-8)
- Matthews, E. C., Mollière, P., Kühnle, H., et al. 2025, *ApJL*, 981, L31, doi: [10.3847/2041-8213/adb4ec](https://doi.org/10.3847/2041-8213/adb4ec)
- McKinney, W. 2010, in *Proceedings of the 9th Python in Science Conference*, ed. Stéfan van der Walt & Jarrod Millman, 56 – 61, doi: [10.25080/Majora-92bf1922-00a](https://doi.org/10.25080/Majora-92bf1922-00a)
- Miles, B. E., Biller, B. A., Patapis, P., et al. 2023, *ApJL*, 946, L6, doi: [10.3847/2041-8213/acb04a](https://doi.org/10.3847/2041-8213/acb04a)
- Mollière, P., Molyarova, T., Bitsch, B., et al. 2022, *ApJ*, 934, 74, doi: [10.3847/1538-4357/ac6a56](https://doi.org/10.3847/1538-4357/ac6a56)
- Mollière, P., Kühnle, H., Matthews, E. C., et al. 2025, *arXiv e-prints*, arXiv:2507.18691, doi: [10.48550/arXiv.2507.18691](https://doi.org/10.48550/arXiv.2507.18691)
- Moran, S. E., Lodge, M. G., Batalha, N. E., et al. 2025, *ApJ*, 994, 116, doi: [10.3847/1538-4357/ae0583](https://doi.org/10.3847/1538-4357/ae0583)

- Mukherjee, S., Batalha, N. E., Fortney, J. J., & Marley, M. S. 2023, *ApJ*, 942, 71, doi: [10.3847/1538-4357/ac9f48](https://doi.org/10.3847/1538-4357/ac9f48)
- Mukherjee, S., Fortney, J. J., Morley, C. V., et al. 2024, *ApJ*, 963, 73, doi: [10.3847/1538-4357/ad18c2](https://doi.org/10.3847/1538-4357/ad18c2)
- Öberg, K. I., Murray-Clay, R., & Bergin, E. A. 2011, *ApJL*, 743, L16, doi: [10.1088/2041-8205/743/1/L16](https://doi.org/10.1088/2041-8205/743/1/L16)
- Pathak, P., Petit dit de la Roche, D. J. M., Kasper, M., et al. 2021, *A&A*, 652, A121, doi: [10.1051/0004-6361/202140529](https://doi.org/10.1051/0004-6361/202140529)
- Penzlin, A. B. T., Booth, R. A., Kirk, J., et al. 2024, *MNRAS*, 535, 171, doi: [10.1093/mnras/stae2362](https://doi.org/10.1093/mnras/stae2362)
- Perrin, M. D., Pueyo, L., Van Gorkom, K., et al. 2018, in *Society of Photo-Optical Instrumentation Engineers (SPIE) Conference Series*, Vol. 10698, *Space Telescopes and Instrumentation 2018: Optical, Infrared, and Millimeter Wave*, ed. M. Lystrup, H. A. MacEwen, G. G. Fazio, N. Batalha, N. Siegler, & E. C. Tong, 1069809, doi: [10.1117/12.2313552](https://doi.org/10.1117/12.2313552)
- Perrin, M. D., Sivaramakrishnan, A., Lajoie, C.-P., et al. 2014, in *Society of Photo-Optical Instrumentation Engineers (SPIE) Conference Series*, Vol. 9143, *Space Telescopes and Instrumentation 2014: Optical, Infrared, and Millimeter Wave*, ed. J. M. Oschmann, Jr., M. Clampin, G. G. Fazio, & H. A. MacEwen, 91433X, doi: [10.1117/12.2056689](https://doi.org/10.1117/12.2056689)
- Phillips, M. W., Tremblin, P., Baraffe, I., et al. 2020, *A&A*, 637, A38, doi: [10.1051/0004-6361/201937381](https://doi.org/10.1051/0004-6361/201937381)
- Rameau, J., Chauvin, G., Lagrange, A.-M., et al. 2013, *ApJL*, 772, L15, doi: [10.1088/2041-8205/772/2/L15](https://doi.org/10.1088/2041-8205/772/2/L15)
- Roellig, T. L., Van Cleve, J. E., Sloan, G. C., et al. 2004, *ApJS*, 154, 418, doi: [10.1086/421978](https://doi.org/10.1086/421978)
- Rouan, D., Riaud, P., Boccaletti, A., Clénet, Y., & Labeyrie, A. 2000, *PASP*, 112, 1479, doi: [10.1086/317707](https://doi.org/10.1086/317707)
- Santos, N. C., Israelian, G., & Mayor, M. 2004, *A&A*, 415, 1153, doi: [10.1051/0004-6361:20034469](https://doi.org/10.1051/0004-6361:20034469)
- Smith, B. A., & Terrile, R. J. 1984, *Science*, 226, 1421, doi: [10.1126/science.226.4681.1421](https://doi.org/10.1126/science.226.4681.1421)
- Soummer, R., Hines, D., & Perrin, M. 2013, *Simulations of target acquisition with MIRI four-quadrant phase mask coronagraph (I)*, Technical Report JWST-STScI-003063
- Soummer, R., Pueyo, L., & Larkin, J. 2012, *ApJL*, 755, L28, doi: [10.1088/2041-8205/755/2/L28](https://doi.org/10.1088/2041-8205/755/2/L28)
- Suárez, G., & Metchev, S. 2022, *MNRAS*, 513, 5701, doi: [10.1093/mnras/stac1205](https://doi.org/10.1093/mnras/stac1205)
- Sudarsky, D., Burrows, A., & Hubeny, I. 2003, *ApJ*, 588, 1121, doi: [10.1086/374331](https://doi.org/10.1086/374331)
- Sudarsky, D., Burrows, A., & Pinto, P. 2000, *ApJ*, 538, 885, doi: [10.1086/309160](https://doi.org/10.1086/309160)
- The pandas development team. 2021, *pandas-dev/pandas: Pandas 1.3.5, v1.3.5 Zenodo*, doi: [10.5281/zenodo.5774815](https://doi.org/10.5281/zenodo.5774815)
- Thorngren, D. P., Fortney, J. J., Murray-Clay, R. A., & Lopez, E. D. 2016, *ApJ*, 831, 64, doi: [10.3847/0004-637X/831/1/64](https://doi.org/10.3847/0004-637X/831/1/64)
- Trifonov, T., Tal-Or, L., Zechmeister, M., et al. 2020, *A&A*, 636, A74, doi: [10.1051/0004-6361/201936686](https://doi.org/10.1051/0004-6361/201936686)
- Turrini, D., Schisano, E., Fonte, S., et al. 2021, *ApJ*, 909, 40, doi: [10.3847/1538-4357/abd6e5](https://doi.org/10.3847/1538-4357/abd6e5)
- Vasist, M., Mollire, P., Kühnle, H., et al. 2025, *arXiv e-prints*, arXiv:2507.12264, doi: [10.48550/arXiv.2507.12264](https://doi.org/10.48550/arXiv.2507.12264)
- Virtanen, P., Gommers, R., Oliphant, T. E., et al. 2020, *Nature Methods*, 17, 261, doi: [10.1038/s41592-019-0686-2](https://doi.org/10.1038/s41592-019-0686-2)
- Visscher, C., Lodders, K., & Fegley, Jr., B. 2006, *ApJ*, 648, 1181, doi: [10.1086/506245](https://doi.org/10.1086/506245)
- Viswanath, G., Janson, M., Dahlgqvist, C.-H., et al. 2021, *A&A*, 651, A89, doi: [10.1051/0004-6361/202140730](https://doi.org/10.1051/0004-6361/202140730)
- Wang, J. J., Ruffio, J.-B., De Rosa, R. J., et al. 2015, *pyKLIP: PSF Subtraction for Exoplanets and Disks*, Astrophysics Source Code Library, record ascl:1506.001
- Waskom, M. L. 2021, *Journal of Open Source Software*, 6, 3021, doi: [10.21105/joss.03021](https://doi.org/10.21105/joss.03021)
- Welbanks, L., Bell, T. J., Beatty, T. G., et al. 2024, *Nature*, 630, 836, doi: [10.1038/s41586-024-07514-w](https://doi.org/10.1038/s41586-024-07514-w)
- Whiteford, N., Glasse, A., Chubb, K. L., et al. 2023, *MNRAS*, 525, 1375, doi: [10.1093/mnras/stad670](https://doi.org/10.1093/mnras/stad670)
- Wogan, N. F., Mang, J., Batalha, N. E., et al. 2025, *Research Notes of the American Astronomical Society*, 9, 108, doi: [10.3847/2515-5172/add407](https://doi.org/10.3847/2515-5172/add407)
- Xuan, J., Ruffio, J.-B., Sanghi, A., et al. 2025, *Combining isotopic and elemental abundances to unveil the formation and accretion history of a cold Jupiter*, JWST Proposal. Cycle 4, ID. #8714
- Zechmeister, M., Kürster, M., Endl, M., et al. 2013, *A&A*, 552, A78, doi: [10.1051/0004-6361/201116551](https://doi.org/10.1051/0004-6361/201116551)